ADVANCED FUNCTIONAL MATERIALS
www.afm-journal.de

Tailoring Photoweldable Shape Memory Polyurethane with Intrinsic Photothermal / Fluorescence Via Engineering Metal-Phenolic Systems

Zhongxin Ping, Fang Xie, Xiaobo Gong, Fenghua Zhang, Jie Zheng, Yanju Liu, and Jinsong Leng**

Multifunctional shape memory polymers are significant for next-generation intelligent systems as smart materials. However, their practical applications are limited by toughness, manufacturability, and functional integration strategies. Besides, while 4D printing is used to construct deformable devices, the limited accessible shapes and difficulty of integrating multiple materials hindered the development of multifunctional devices. Herein, metal-phenolic coordination is used as crosslinks to tailor tough shape memory polyurethanes with intrinsic photothermal effect and/or tunable fluorescence. The reversible dissociation of metal-phenolic complexes upon loading provides an efficient energy dissipation for the polymer network. The photothermal/fluorescent properties of target polyurethane can be effortlessly programmed by changing the coordinated metals and functional ligands. The obtained fluorescent polyurethane displays tunable fluorescence through the reversible dissociation-association of dynamic bonds upon thermal stimulus. Moreover, relying on light-triggered hybrid exchange reactions among various metal-phenolic coordination bonds, heterogeneous interfaces can be merged to manufacture exquisite 3D shape-shifting devices and integrate more advanced functions. As demonstrations, intrinsic photothermal-responsive shape memory stent, and 3D fluorescent encryption device are produced based on photo-welding instead of 4D printing. This study not only provides a convenient supramolecular strategy for constructing multifunctional smart materials but also demonstrates a feasible method for making personalized integrated architectures.

1. Introduction

Shape memory polymers (SMPs) were a classic smart deformable material that showed great potential in shape-shifting-related intelligent systems such as anti-counterfeiting, information encryption, and biomedicine.[1] Most SMPs were only thermal-responsive, and heat conduction often made it difficult to precisely control their shape recovery during direct heating. In contrast, the deformation of photothermal-responsive SMPs could be remotely and precisely guided in space and time through light stimuli.[2] Furthermore, advanced SMPs were required to integrate multiple functions to meet diverse application requirements. For example, SMP-based 3D information encryption platforms showed great potential in the field of anti-counterfeiting. However, information storage achieved through only by deformation may lead to information leakage under destructive processing. Tunable fluorescence was a fascinating property that can change in response to external stimuli, providing the opportunity to display information on demand in information encryption platforms.[3] Therefore, to enhance the application security and timeliness of the information encryption platform, SMPs needed to be integrated with tunable fluorescence. 3D structures composed of various functional polymers have attracted much attention in fields such as soft robotics, tissue engineering, and deployable devices.[4] To achieve flexible morphology design and integration of advanced functions in deformable devices, it was inevitable to merge heterogeneous functional polymers, which put forward requirements for the dynamic characteristics of crosslinking networks.[5] Therefore, developing multifunctional dynamic polymer networks was of profound significance but fraught with difficulties.

A wide range of strategies for integrating photoresponsive functions in SMPs has been developed and they could be divided into two major categories: i) adding photothermal or fluorescent fillers to the polymer matrix to prepare composites,[6] and ii) regulating molecular architectures to prepare intrinsic

Z. Ping, F. Zhang, J. Leng
Center for Composite Materials and Structures
Harbin Institute of Technology
Harbin 150080, P. R. China
E-mail: lengjs@hit.edu.cn
F. Xie, X. Gong, J. Zheng
Department of Materials Science and Engineering
Harbin Institute of Technology at Weihai
Weihai 264209, P. R. China
E-mail: fangxie@hit.edu.cn
Y. Liu
Department of Astronautical Science and Mechanics
Harbin Institute of Technology
Harbin 150001, P. R. China

The ORCID identification number(s) for the author(s) of this article can be found under https://doi.org/10.1002/adfm.202402592

DOI: 10.1002/adfm.202402592

photoresponsive SMPs.[7] For the former, functional fillers, such as photothermal fillers (MXene, graphene, carbon nanotubes, and Fe_3O_4 nanoparticles), and fluorescent fillers (perovskite quantum dots, carbon dots, and fluorescent dyes), were often inevitable in uncontrollable aggregation.[8] Such undesirable aggregation resulted in poor mechanical properties and photoresponsive functionality. Moreover, some functional additives had poor biodegradability and potential toxicity, making it difficult to apply such shape memory composites in the biomedical field.[9] The latter approach was widely implemented, as it could offer flexibility and opportunities to tailor SMPs with strong mechanical properties and multi-functions. However, designing molecular architectures to achieve functional integration often involves complex synthetic strategies. Molecular architectures for functional integration and energy dissipation were difficult to couple, resulting in a trade-off between mechanical properties, and functionality of polymer networks.[10] Therefore, it was of great significance to develop a convenient and efficient strategy for engineering tough SMPs with well-defined functions.

Introducing molecular architectures with desired functions to partake in crosslinking was an effective means to produce target functional polymers.[11] Metal-phenolic system (MPS) was a supramolecular network structure composed of metal ions (such as Fe^{3+}, Eu^{3+}) and phenolic ligands (such as natural or synthetic polyphenols).[12] Modulating metal ions and ligands has become a universal strategy to prepare MPS with specific functions, such as fluorescence,[13] photothermal effect,[14] self-destruction,[15] antibacterial,[16] and adhesion.[17] However, previous refreshing studies on metal-phenolic networks had only focused on functional nanoparticles, coatings, and hydrogels. MPS-cored polymeric films with multi-functions and high toughness had been less developed. Considering the numerous advantages of MPS, introducing MPS as a crosslinking component may be a feasible and promising method to prepare polymeric films with both excellent mechanical properties and well-defined functions. Moreover, relying on the good biodegradability of MPS, it was expected that versatile MPS-cored SMPs would have broad application prospects in biological applications.

Herein, we reported a strategy for preparing functionalized polymers based on metal-phenolic systems. Specifically, MPS was used as crosslinking to prepare multifunctional shape memory polyurethanes with intrinsic photothermal or/and tunable fluorescence (**Scheme 1**). The intrinsic photothermal/fluorescent properties of polymer networks can be tailored by changing metal ions and guest ligands. The dynamic metal-phenolic coordination bonds provided effective energy dissipation for the polymer network when strained. Based on the intrinsic photothermal effect, the heterogeneous metal-phenolic coordination bonds originating from various polymers can be dissociated and recombined to merge overlapping interfaces, thereby achieving photo-welding. Various impressive deformable devices composed of heterogeneous functional polyurethanes were fabricated using photo-welding instead of 4D printing. Light-triggered shape memory vascular stents made by photo-welding may provide a guarantee for emergency rescue scenarios. Photo-welded 3D fluorescent encryption device relying on localized shape memory behavior to achieve decryption provided a reference for the rapid design and manufacturing of advanced information encryption platforms. This study provided a robust supramolecular strategy for producing multifunctional smart materials and a convenient approach for manufacturing personalized sophisticated architectures.

2. Results and Discussion

2.1. Construction and Characterization of the PU-PM

Considering the good biocompatibility and degradability of metal-phenolic systems and the huge demand for SMPs in biomedicine,[18] wearable devices,[19] and 4D printing,[20] degradable and biosafe polycaprolactone (PCL) was selected as a soft segment to build the SMP network. Functionalized shape memory polyurethane was prepared using the prepolymer method (**Figure 1a**). Polycaprolactone diol (PCL-2OH; -OH) was reacted with hexamethylene diisocyanate (HDI; -NCO) for 20 h to obtain -NCO-terminated molecular chains. Then, a yellow-green solution was subsequently obtained after the 3,4-dihydroxybenzaldehyde (PA; -OH, and Salvia miltiorrhiza extract) as a chain extender was added to the resulting product at 70 °C for 24 h. Then, the solution was mixed with different coordinated metals, obtaining polyurethane (PU) film with shape memory, and intrinsic photothermal effect (denoted as PU-PM; PU-PM represented the general name for metal ions-coordinated PUs). The method of integrating fluorescence function was unique, and the synthesis and characterization of photoluminescent PU were separately discussed in subsequent chapters.

Different metal-phenolic crosslinking defined the color of the PU films. Compared with the light-yellow PU-PA (uncoordinated PU) film, PU-PFe (Fe^{3+}-coordinated PU) film appeared deep black, while the color of PU-PEu (Eu^{3+}-coordinated PU) film deepened to dark yellow (Figure 1a, inset). The large differences in color transitions can be attributed to the different electronic structures of the heterogeneous coordinated metals.[21] Fourier-transform infrared (FTIR) spectra and nuclear magnetic resonance (NMR) spectra were used to confirm the successful preparation of PU-PA (Figure 1b; Figure S1, Supporting Information). The peak of the -NCO group near 2273 cm^{-1} was not observed, indicating that the phenolic hydroxyl group successfully participated in the condensation reaction. Moreover, adding metal ions resulted in a decreased intensity of the HO—C stretching peak at 1529 cm^{-1}, indicating the formation of metal-phenolic coordination bonds. The coordination patterns of metal-phenolic complexes presented strongly pH-dependent self-assembly kinetics.[22] Raman and UV–vis spectra were used to elucidate the coordination modes of metal-phenolic crosslinking. Compared with uncoordinated PU-PA, peaks related to the vibration of metal-catechol bonds were detected in the Raman spectra of PU-PM in the range of 480–660 cm^{-1}, further confirming the formation of coordination crosslinking (Figure 1c; Figure S2, Supporting Information). Furthermore, the peak at 535 cm^{-1} of PU-PFe was related to the increased bis- and tris-catechol-Fe (III) complexes relative to the mono-catechol-Fe (III) complex, confirming the dominance of bis- and tris-complexes. The presence of broad ligand-to-metal charge-transfer (LMCT) bands in the UV–vis spectra of PU-PM further indicated the formation of metal-phenolic crosslinking (Figure 1d). The metal compound precipitation was not detected by Scanning electron microscopy

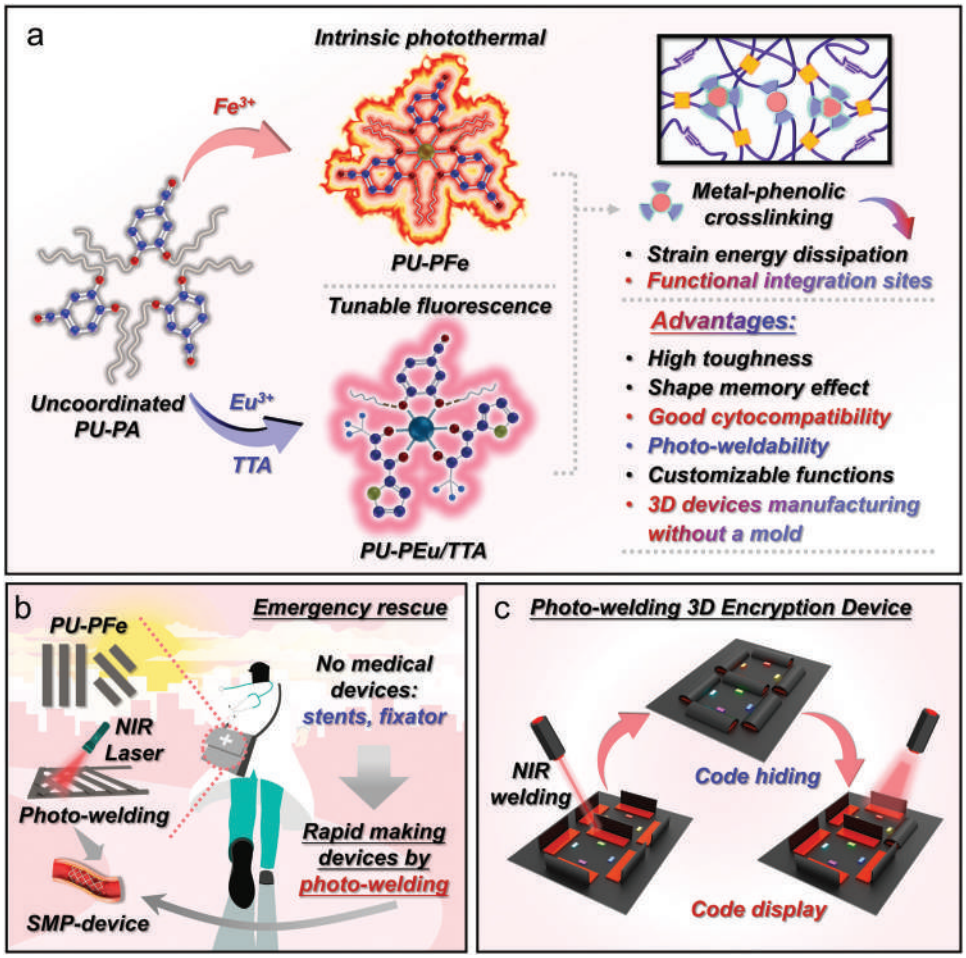

Scheme 1. a) Schematic illustration of the engineering shape memory polyurethane with intrinsic photothermal/fluorescent properties based on the metal-phenolic system. b) Diagram of rapidly making shape memory medical devices composed of PU-PFe films for emergency rescue via photo-welding. c) Illustration of easily assembling various functional PU films into a 3D information encryption device through photo-welding.

(SEM) and energy-dispersive X-ray spectroscopy (EDX) at the microscale. The metal elements were evenly distributed in the PU films (Figure S3, Supporting Information). Besides, no diffraction peaks corresponding to any inorganic compound were observed in the X-ray diffraction spectra (XRD) (Figure S4, Supporting Information). Therefore, the contribution of inorganic fillers to the mechanical properties of the polymer network was excluded.

2.2. Toughening Effect and Mechanism of PU-PM

Uniaxial tensile testing was used to explore the mechanical properties of PU-PA, PU-PFe, and PU-PEu with a stretching rate of 30 mm min^{-1} at room temperature (**Figure 2**a,b; Figure S5, Supporting Information). The PU-PA had the worst mechanical properties (average toughness: 96 MJ m^{-3}), which can be attributed to the brittleness caused by the high crystallinity of the sequential linear polymer network. In comparison, PU-PM, with metal-phenolic crosslinks, had much stronger mechanical properties. The engineering stress, engineering strain, and toughness had been greatly improved. Especially, PU-PFe represented 3.25 fold higher engineering stress (52.7 MPa), 1.79 fold higher engineering strain (1515%), and 3.79 fold higher toughness (364 MJ m^{-3}) than uncoordinated PU-PA. Note that the engineering stress of PU-PFe was higher than that of PU-PEu, which may be contributed by the difference in bond energy of heterogeneous metal-phenolic coordination bonds. Typical true stress-strain curves for PU films were used to complement the engineering stress-strain curves (Figure 2c). The true stresses of PU-PFe and PU-PEu were as high as 888.58 and 630.47 MPa, respectively. Moreover, PU-PFe flake (0.0123 g) could load 2.975 kg of weight (241869 times the film weight; Figure 2c inset), which further revealed the remarkable mechanical robustness of PU-PFe film. Compared with previously reported photothermal polymeric composites,[6a,23] intrinsic photothermal polymers,[9b,24] and luminescent polymers,[11a,25] PU-PM with designable integrated functions exhibited excellent comprehensive mechanical properties (Figure 2d).

Then, the crystalline and phase separation of PU films were explored to clarify the effect of coordination crosslinking on the polymer structure. The wide-angle X-ray diffraction (WAXD)

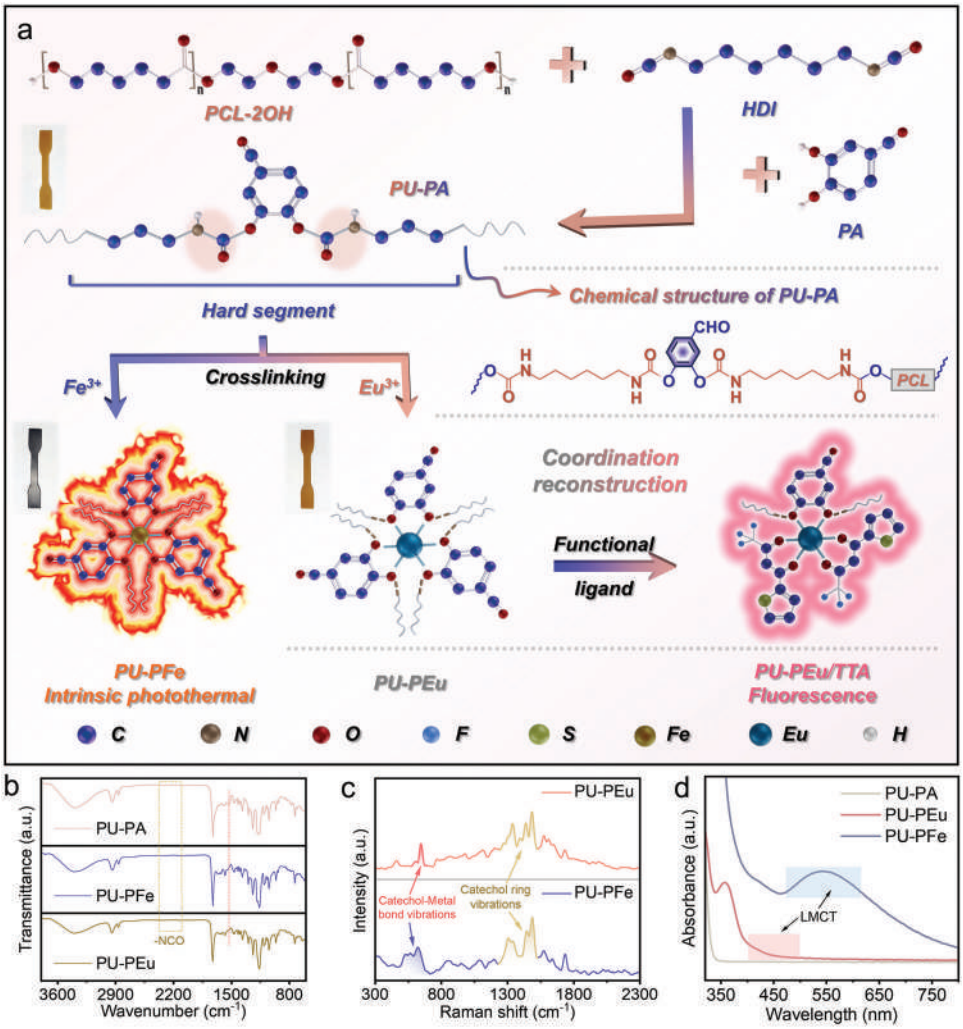

Figure 1. Synthesis routes and characterization of PU-PMs. a) Schematic illustrating the synthesis of PU-PMs. b) FTIR spectra, c) Raman spectra, and d) UV–vis spectra of different PU-PMs.

pattern of PU-PA appeared sharp crystal reflections at $2\theta = 21°$ and 23.6°, corresponding to the (110) and (200) planes of PCL respectively (Figure S4, Supporting Information).[26] Nevertheless, the WAXD patterns of PU-PFe and PU-PEu presented two broad and low diffraction peaks, indicating that amorphous PCL was dominated in the polymer network. The explanation for this was that introducing metal-phenolic crosslinking destroyed chain ordering and inhibited the crystallization of PCL, which was verified by differential scanning calorimetry (DSC) (Figure S6, Supporting Information).[27] Compared with the melting peaks of PU-PA (melting temperature (T_m): 54.8 °C), that of PU-PFe and PU-PEu (T_m: 47.5 °C) moved to the lower temperature and presented a broader peak width. The crystallinity of PU-PA (ca. 39.9%) was much higher than that of PU-PFe (ca. 23.7%) and PU-PEu (ca. 26.4%), which confirmed the hindering of crosslinking on crystallization behavior. Note that the similarity in crystallinity between PU-PFe and PU-PEu may be an important factor in their similar mechanical properties. Moreover, these results meant that the shape memory effect of PU-PM was dependent on the melting-crystallization behavior of PCL segments.

The small-angle X-ray scattering (SAXS) patterns were used to investigate the microphase-separated structure in PU-PFe induced by coordination bonds and hydrogen bonds. The periodicity of the phase separation domains was calculated to be ≈13.74 nm (Figure S7, Supporting Information). For this, we hypothesized that multiple noncovalent interactions (metal-phenolic coordination bonds and hydrogen bonds) were confined within the crystalline PCL to generate phase-separated domains with hierarchical structures (Figure S8, Supporting Information).

The structural evolution of phase separation domains was analyzed based on WAXD and 2D-SAXS patterns of PU-PFe under different degrees of strain to elucidate the toughening mechanism (Figure 2e,f). When the film was stretched to 150% strain, the intensity of the diffraction peak of the crystalline PCL increased slightly in the WAXD patterns. However, 2D-SAXS images displayed that the isotropic scattering underwent a round-to-rhombus change. This indicated that the phase separation domain deformed at 150% strain and a low degree of strain-induced crystallization (SIC) occurred inside the film. When stretched to 300% strain, the intensity of the diffraction peak of the crystalline

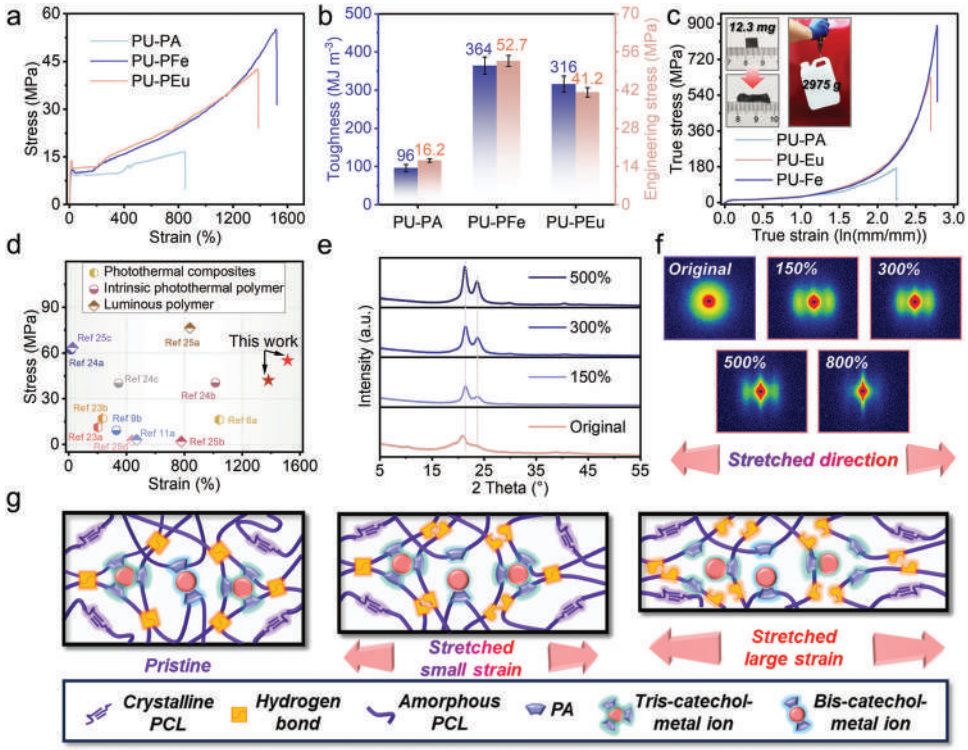

Figure 2. Mechanical properties and toughening mechanism of PU-PM. a) Engineering stress-strain curves of PU-PM. b) Toughness comparison of different PU films. c) True stress-strain curves of PU-PM. d) Comparison between PU-PFe/PU-PEu and previously reported functional polymers or composites in terms of stress and strain. e) WAXD and f) 2D-SAXS patterns of PU-PFe at different strains. g) Schematic of the mechanism of enhanced mechanical properties of PU-PFe with metal-phenolic crosslinking.

PCL increased significantly in the WAXD patterns. Meanwhile, the 2D-SAXS pattern had no obvious change compared with the previous stage. The intensity of the scattering peak in the 1D-SAXS profiles decreased slightly (Figure S7, Supporting Information). This confirmed that the structure of phase-separated domain still remained relatively intact. However, the strain process induced the elongation, arrangement, and alignment of molecular chains, which led to a high degree of SIC. When stretched to 500% strain or even higher, the intensity of scattering pattern in SAXS decreased greatly. This moment, the coordination bond and hydrogen bond were rapidly destroyed, indicating that the structure of phase separation domains gradually collapsed. The dissociation energy of the Fe (III)-phenolic coordination bond was much higher than that of the hydrogen bond.[28] As shown in Figure 2g. when stretched to small strains, hydrogen bonds with lower dissociation energy dissociated first. As the strain increased further, Fe (III)-phenolic coordination bonds dissociated. The external mechanical stress caused the non-covalent bonds to dissociate and reorganize at newly accessible segments, resulting in superior energy dissipation. Combining the above, the remarkable mechanical properties of PU-PFe can be attributed to several factors: i) the microphase separation domain acted as a rigid nanofiller; ii) the Fe (III)-phenolic coordination bond strengthened the energy barrier for chain separation from the domain; iii) the dissociation-recombination behavior of hierarchical dynamic non-covalent bonds greatly improved the energy dissipation.

2.3. Photoweldability and Light-Triggered Shape Memory Based on Intrinsic Photothermal Effect

The intrinsic photothermal effect was of great significance for photo-welding and light-triggered shape memory. The photothermal conversion mechanism of MPS-based PU-PM adhered to the fundamental principle of "light absorption – electronic transition – vibrational relaxation (heat generation)" (Figure S9, Supporting Information).[29] Superior light absorption will lay the foundation for the intrinsic photothermal effect of PU films.[30] As shown in **Figure 3**a, the UV–vis-near infrared (UV–vis-NIR) absorption spectra were used to investigate the light absorption of various PU films. The PU-PFe and PU-PEu films exhibited stronger light absorption over the pure PCL and uncoordinated PU-PA films in the short-wavelength near-infrared region. The absorption of PU-PFe and PU-PEu at 808 nm were 96.1% and 75.5%, respectively. Note that the light absorption of PU-PFe was much higher than that of PU-PEu. The changing trend of the light absorption of the PU films matched their color change trend (Figure 1a, insets). This can be attributed to the following factors: Fe^{3+} with partially filled d orbitals formed deep black Fe (III)-phenolic crosslink with strong light absorption due to the d–d transition; conversely, due to the subtle bandgap changes of the f–f transition, Eu^{3+} formed light-colored Eu (III)-phenolic crosslink.[21] These unique properties of MPS also provided the possibility to customize PU films with different colors and optical properties.

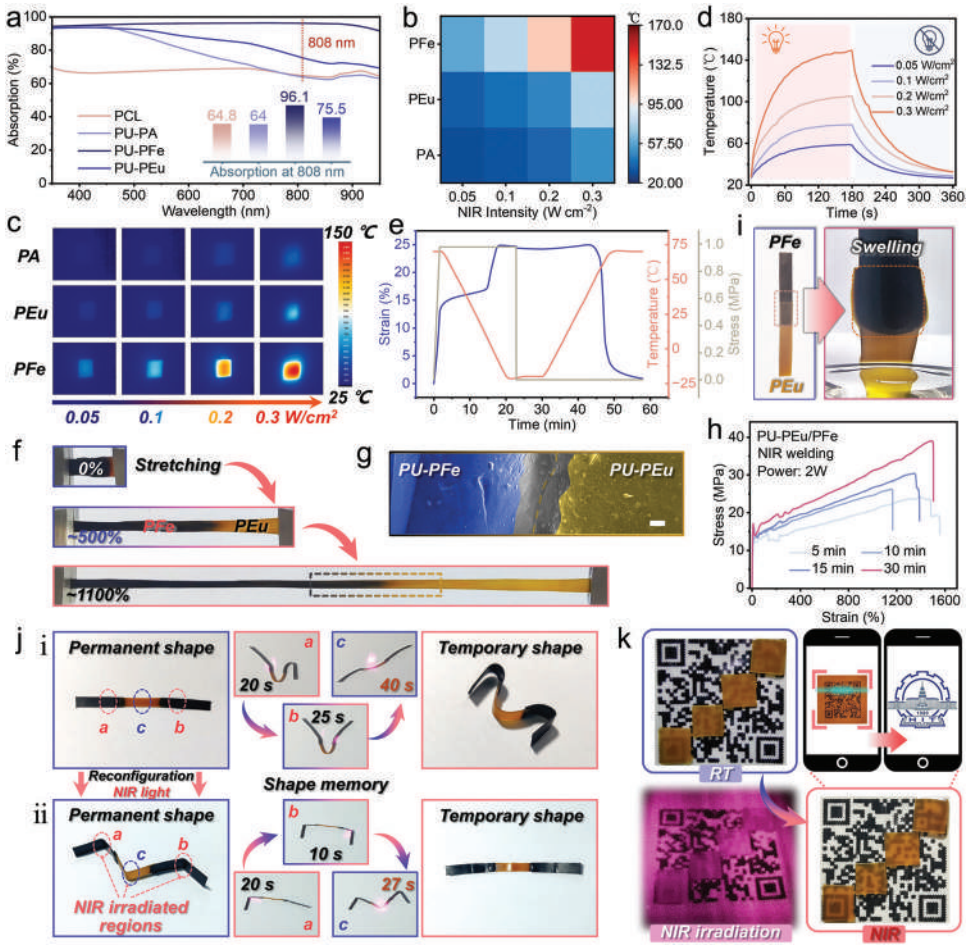

Figure 3. Intrinsic photothermal performance, photo-welding, and light-triggered shape memory. a) UV–vis-NIR absorption spectra of different PU films. b) Surface equilibrium temperature of various PU films with different NIR intensities. c) IR images of various PU films irradiated with various NIR intensities. d) Time-dependent temperature profiles of PU-PFe recorded under NIR on-off of various intensities. e) Dynamic mechanical analysis curve of PU-PFe film in shape memory behavior. f) Photographs of stretching PU-PFe/PEu welded for 15 min to various strains (ca. 0%, 500%, 1100%). g) SEM images of PU-PFe/PEu after welding (The scale bar was 100 μm). h) Stress-strain curves of PU-PFe/PEu samples at different times of welding (5, 10, 15, and 30 min). i) Swelling experiments in THF of photo-weld PU-PFe/PEu. j) Process of multistage NIR-triggered shape memory behavior and permanent shape reconfiguration properties of welded PU-PFe/PEu/PFe film. k) The applications of PU-PEu film used for information identification.

Subsequently, the photothermal performance of these PU films was surveyed in detail. Under the vertical 808 nm NIR irradiation with the same power density, uncoordinated PU-PA displayed the lowest equilibrium temperature, while PU-PFe exhibited the highest equilibrium temperature (Figure 3b,c). When the NIR irradiation intensity was 0.05, 0.1, 0.2, and 0.3 W cm^{-2}, the maximum steady-state temperatures of PU-PFe reached 58.3, 77.8, 105.5, and 149.3 °C within 180 s, respectively. Notably, the photothermal equilibrium temperatures of various PU films were positively correlated with the NIR power density, which meant that the surface temperature could be regulated remotely by changing the NIR power. This laid a good foundation for succeeding photo-welding and light-triggered shape memory effects. The surface temperature of PU-PEu with relatively low light absorption reached 75 °C under the NIR irradiation (0.3 W cm^{-2}), which was higher than the shape memory transition temperatures (T_{trans}) (ca. 47.5 °C). When exposed to NIR irradiation, the U-shaped PU-PEu film could recover to its original linear shape (Figure S10, Supporting Information). Besides, the surface temperature would gradually return to room temperature within 3 min after the highly focused NIR irradiation was stopped (Figure 3d). This rapid natural cooling property can facilitate shape fixation in shape memory and maneuverability during photo-welding.

The metal-phenolic crosslinking and melting-crystallization behavior endowed PU films with a satisfactory shape memory effect. Taking PU-PFe as an example, the one-way shape memory effect of PU-PFe was investigated. When the temperature exceeded T_{trans}, melting of the crystallized PCL resulted in a remarkable increase in the mobility of the PU chains. At this moment, programming the temporary shape can be accomplished by applying external loads. After cooling to room temperature and removing external loads, recrystallization of PCL resulted in a significant decrease in chain mobility, and the temporary shape was fixed. Driven by entropic elasticity, the deformed sample would return to its original shape when the temperature was

reheated above T_{trans} without external loads. (Figure S11, Supporting Information). DMA in controlled force mode was used to record the single shape memory process of PU-PFe, including shape programming, cooling, shape fixation, and shape recovery (Figure 3e). Note that PU-PFe underwent strain elongation during cooling caused by the crystallization-induced elongation (CIE) effect. The shape fixation rate (R_f) and shape recovery rate (R_r) of PU-PFe were calculated from Equations S1 and S2 (Supporting Information) (See detailed in Figures S1–S6, Supporting Information) to be 98% and 93%, respectively. The shape memory curves of PU-PEu and PU-PEu/TTA showed that their R_f were both higher than 98%, and their R_r were both higher than 94% (Figure S12, Supporting Information). These results revealed that the prepared photoresponsive PUs had superior shape memory properties.

Merging heterogeneous polymers based on photo-welding was of great significance for realizing flexible morphological design, multifunctional integration, and independent control of different modules of exquisite 3D structures.[31] The intrinsic photothermal effect and dynamic crosslinking of PU-PM made it possible to manufacture ingenious devices constructed of heterogeneous functional interfaces through photo-welding. Stress relaxation curves indicated that PU-PM had good dynamic properties (Figure S13, Supporting Information). Attributed to the rapid exchange of metal-phenolic coordinate bonds at high temperatures, the stress relaxation of the PU-PM became more rapid with increasing temperature. 808 nm NIR light irradiation (input power: 2 W) was used to weld the overlapping regions of PU-PFe and PU-PEu to obtain PU-PEu/PFe film. Note that all types of PU films showed good thermal stability, which provided a guarantee for the stable implementation of photo-welding (Figure S14, Supporting Information). As expected, the PU-PEu/PFe film exhibited superior stability after undergoing NIR welding. There was no separation observed in the weld region during stretching (Figure 3f). The scanning electron microscopy (SEM) image showed an overall and unified shape at the weld region (Figure 3g). When stretching to fracture, the breaks occurred on a single film or at the edge of the welding region (Figure S15, Supporting Information). These indicated that there was robust interface bonding at the welding region of PU-PEu/PFe film. To quantitatively investigate the photo-welding efficiency, the mechanical properties of the welded PU-PEu/PFe were measured through tensile testing (Figure 3h). The results displayed that the mechanical properties of the welded PU-PEu/PFe gradually increased with the increase of photo-welding time. The raised temperature greatly enhanced the mobility of PU molecular chains, providing the driving force to bypass kinetic traps. Consequently, the overlapping heterogeneous PU interfaces snugly aligned and firmly merged through the dissociation-hybrid association of metal-phenolic coordination bonds (Figure S16, Supporting Information). The weld region was bent after swelling in tetrahydrofuran (THF) for 24 h, which may be caused by the difference in swelling ratio between heterogeneous PU films (Figure 3i). The weld region did not collapse due to interfacial stress, further indicating the formation of stable hybrid coordination bonds between heterogeneous films.

The practical applications of 3D deformable devices composed of SMPs inevitably required precise shape control in specific areas, which was difficult to achieve by activating shape recovery by direct heating. The good photothermal performance of PU-PM laid the foundation for precise shape control. Two pieces of PU-PFe and one piece of PU-PEu films were merged sequentially by photo-welding, and the obtained photo-welded sample was named PU-PFe/PEu/PFe (Figure 3j; Figures S1–S7, Supporting Information). For the shape programming process, the NIR laser was used to irradiate the three target sites (sites "a", "b", and "c") of the PU-PFe/PEu/PFe film sequentially to increase the mobility of molecular chains. Note that due to differences in photothermal performance, the NIR light power density to irradiate PU-PFe (sites "a" and "b", 0.2 W cm^{-2}) and PU-PEu (site "c", 0.4 W cm^{-2}) was different. Meanwhile, an external load was applied to bend this film. Subsequently, the welded film was naturally cooled to room temperature under external load to fix the temporary shape. After programming the three deformation sites, an M-shaped PU-PFe/PEu/PFe film was obtained. Photo-welded PU-PFe/PEu/PFe film exhibited great advantages in controlled shape recovery. By defining the irradiation regions, the film with the temporary shape M can achieve precise control of shape recovery at various positions at specified time nodes (Figure 3j–i). Specifically, under NIR light irradiation (0.2 W cm^{-2}), sites "a" and "b" located on the PU-PFe film recovered their permanent shapes within 25 s; site "c" (0.4 W cm^{-2}) located on the PU-PEu film recovered original linear shape after being irradiated with NIR light for 40 s. Note that the difference in the photothermal performance of the two films led to differences in the shape recovery rates at different deformation sites.

Furthermore, the permanent shape of the PU-PFe/PEu/PFe can be reconFigure d relying on the rapid stress relaxation behavior (Figure 3j-ii). The permanent shape of the target region can be rapidly reshaped using NIR irradiation. First, an external load was applied to the target site to cause the film to bend. Subsequently, NIR light was used to illuminate the stress concentration region for a period of time to achieve the shape reconfiguration under external load. The light-triggered shape reconfiguration of both films was affected by the photothermal performance. Under the NIR light irradiation with the same power density (ca. 8 W cm^{-2}), the PU-PFe film can achieve shape reconstruction within 10 s, while PU-PEu needed to achieve this process within 30 s. The original linear PU-PFe/PEu/PFe can be quickly reshaped into an M-shaped film and still maintained shape memory properties. This ultrafast regioselectivity permanent shape reconfiguration would facilitate the rapid manufacturing of complex 3D devices. The PU-PFe/PEu/PFe film with a linear temporary shape after programming exhibited a better shape recovery rate after being irradiated with NIR light at the same power density as mentioned above. This phenomenon can be attributed to the difference in stress concentration between angular deformation and arc deformation. The shape recovery state of PU-PFe and PU-PEu films under the same light intensity can be predicted based on the photothermal performance. When the NIR power density was higher than 0.05 W cm^{-2} and lower than 0.3 W cm^{-2}, only the PU-PFe film underwent the shape recovery; when the NIR power intensity was higher than 0.3 W cm^{-2}, both PU-PFe and PU-PEu films would recover their permanent shape. Therefore, it was feasible to achieve independent control of different parts in the overall welded sample by adjusting the power density of the large-area light source. Note that the NIR power density driving the shape memory process needed to be much

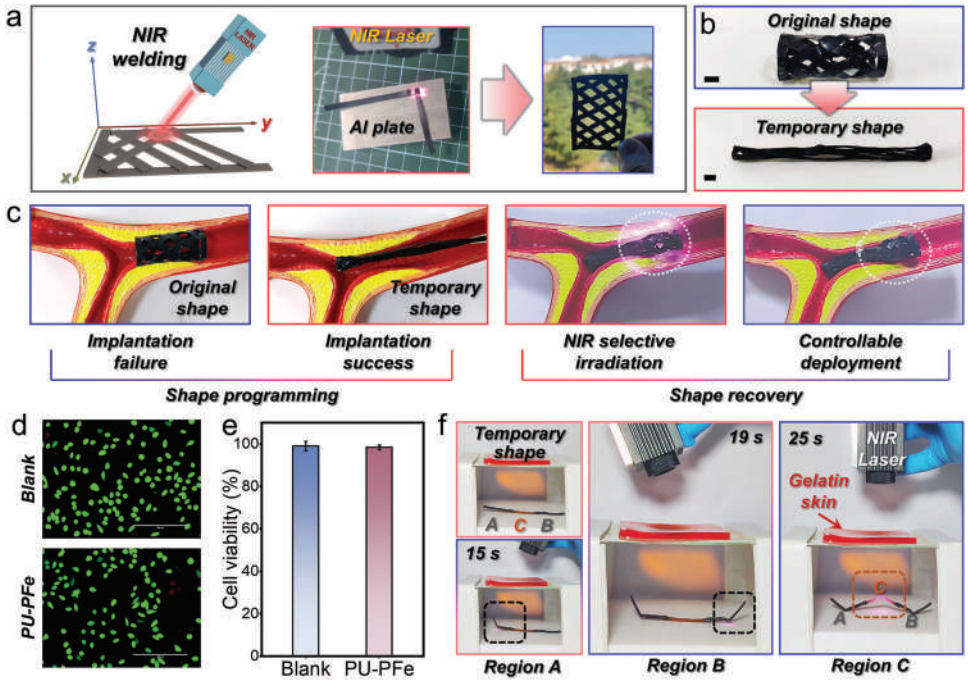

Figure 4. Illustration of the controllable deployment process of photo-welded stent and its cytocompatibility. a) Fabrication process and photographs of 3D stent by photo-welding without a mold. b) Photographs of the shape memory process of photo-welded 3D stent (The scale bar was 5 mm). c) Photographs of simulated stent implantation and NIR-triggered deployment. d) Fluorescent images of the fibroblast cells cultured in PU-PFe and control for 24 h, living cells: green; dead cells: red (The scale bar was 200 μm). e) Cell viability of fibroblasts cultured in control and PU-PFe for 24 h. f) NIR-triggered shape recovery of photo-welded W-shaped structure composed of PU-PFe and PU-PEu under the gelatin skin.

lower than that used during photo-welding to avoid undesirable interface merging during shape manipulation.

Given that PU-PEu was a semi-crystalline SMP at room temperature, the crystallization and melting of PCL resulted in changes in visible light absorption. The temperature-induced change in light transmittance implied the potential of PU-PEu in information recognition and hiding. Figure 3k demonstrated the activation and hiding of QR code information by the PU-PEu film relying on the photothermal effect. At room temperature, the presence of crystals reduced visible light transmittance, thereby hiding the QR code information. After being NIR irradiated (power: 3 W) for 10 s, the crystals in PU-PEu melt and the hidden QR code information can be identified by the mobile phone. The mobile phone can scan the displayed QR code to instantly decode the message "Harbin Institute of Technology's school badge image".

Personalized customization of medical devices with complex shapes in the biomedical field had profound significance for disease treatment.[32] 4D printing offered the opportunity to create deformable medical devices. However, special printers and tedious modeling made the rapid manufacturing of devices in some emergency scenarios difficult. Excitingly, photo welding with spatial selection capability provided a promising approach to the rapid fabrication of non-precision 3D deformable structures. The combination of 3D photo-welding and light-triggered shape memory offers the advantage of a time window compared with 4D printing. As a demonstration, the implantation and light-triggered deployment process of shape memory vascular stent based on photo-welding was demonstrated (**Figure** 4a). This vascular stent was welded from 17 pieces of pre-cut PU-PFe films, which included 50 welding nodes. After heating, transverse stretching caused the vascular stent to shrink in the radial direction (Figure 4b). After cooling to room temperature and removing external forces, the elongated temporary shape was fixed. Figure 4c demonstrated that the intrinsic photothermal effect provided a key operating window for the precise deployment of vascular stents into the human body. Body temperature-triggered shape memory stents can deploy prematurely during deployment leading to implantation failure.[33] In contrast, the 3D photoresponsive shape memory stent prepared based on photo-welding could be deployed regionally through NIR irradiation after implantation and had flexible maneuverability.

After implantation, biocompatibility was necessary for safe implantation of biomedical devices. The cytocompatibility of PU-PFe was evaluated using in vitro fibroblast culture. The fluorescence image of fibroblasts cultured in a culture dish containing PU leachate for 24 h was shown in Figure 4d. Live and dead cells were stained green and red, respectively. After 24 h, there was no significant difference in cell density between the control group and the experimental group, indicating that the PU-PFe had no significant effect on cell proliferation. Cell viability showed that the cell survival rate was over 99% after 24 h, indicating that the PU-PFe had good cytocompatibility and was expected to be used in biomedicine (Figure 4e). Furthermore, using gelatin (ca. 5 mm) as a skin tissue analog, the NIR-triggered shape recovery of PU-PM under skin-like tissue was investigated to elucidate its potential in biomedical applications (Figure 4f). NIR laser (808 nm) can penetrate skin-like tissue and selectively activate

samples in a linear shape (Temporary shape). It can be seen that the "A/B/C" region in the metastable state sequentially recovered its original shape (within 25 s for each node). These results indicated that PU-PM was promising for biomedical applications.

Moreover, NIR-triggered shape memory and ultrafast shape reconfiguration endowed deformable structures with the ability to mimic biological behaviors. As shown in Figure S17 (Supporting Information), based on NIR-triggered shape memory, the photo-welded 2D planar tree structure (Permanent shape 1) can be transformed into a temporary shape resembling a standing deer (Temporary shape 1). Next, the selective shape recovery allowed the standing deer to switch to a half squatting state (Temporary shape 2). Finally, relying on NIR-triggered reshaping capabilities, the half squatting deer transformed into a crouching state (Permanent shape 2). Besides, a 3D morphing aircraft composed of PU-PEu and PU-PFe was fabricated through photo-welding (Figure S18, Supporting Information). Depending on NIR-triggered shape memory, the wing of the morphing aircraft can be adjusted to simulate the flexible flight attitude of bird. Compared with directly heating merged regions with an electric soldering iron,[5a] photo-welding with heat localization ensured the overall orientation during the manufacturing process of welded structures. Photo-welding heterogeneous functional polymer interfaces paved the way for developing multifunctional 3D devices.

2.4. PU-PEu/TTA with Tunable Fluorescence Based on Coordination Reconstruction

Smart fluorescent materials with shape configuration capability were significant for diverse applications, such as fluorescent nanothermometers, information encryption, and anti-counterfeiting.[34] Whereas, most existing fluorescent materials belonged to hydrogel or organo-gel systems, which were susceptible to external physical damage and dehydration, thus restricting their lifespan and reliability. Metal-phenolic coordinate polymers can be imparted with photoluminescence properties by doping functional ligands. Fluorescent PU film was achieved by swelling in a solution containing functional ligands. As shown in **Figure 5**a and 2-thienoyltrifluoroacetone (TTA) was used as a functional coligand to participate in coordination reconstruction to endow the film with fluorescent properties and to prove that the target functions can be integrated into the polymer networks by introducing guest ligands. Specifically, due to the rapid swelling behavior, the film was immersed in a solution containing the Eu-TTA ligand for swelling to doping the functional ligand (Figure S19, Supporting Information). The ligand molecule was then anchored by a thermal-triggered metal-ligand bond recombination. The optimal excitation wavelength of the material was fixed at 365 nm based on fluorescence spectrophotometry (Figure S20, Supporting Information). The PU-PEu/TTA (fluorescent PU doped with TTA) exhibited red fluorescence excited 365 nm UV light (Figure 5a, right). The incorporation of TTA within PU-PEu backbones was investigated by FTIR spectra (Figure 5b). The enhanced intensity of the C=O stretching vibration peak at 1621 cm^{-1} revealed that TTA was successfully bound through coordination. Figure 5c showed the fluorescence spectra of the films before and after doping with TTA. The red fluorescence of PU-PEu/TTA film was mainly attributed to the $^5D_0 \rightarrow {}^7F_2$ transition near 619 nm.[35] The red fluorescence of PU-PEu/TTA corresponded to the expected color of CIE coordinates (0.655, 0.316) (Figure 5d).

Excitingly, the PU-PEu/TTA film exhibited thermal-responsive tunable fluorescence intensity (Figure 5e). As shown in Figure 5f, the fluorescence intensity of the PU-PEu/TTA gradually decreased with increasing temperature until it was quenched. After the temperature dropped to room temperature, the fluorescence intensity would return to its original state. Tunable fluorescence was attributed to the fact that increasing temperature led to the loss of the "antenna effect" and the enhancement of non-radiative transitions.[36]

Shape memory polymers inevitably needed to deform during application, so it was extremely crucial to understand the sensitivity of fluorescence properties to external mechanical stress. The PU-PEu/TTA film can still maintain its uniformly and red fluorescence when strained (Figure 5g). Sustaining excellent fluorescence properties during the straining can provide a guarantee for the shape programming. Furthermore, doping functional ligands did not lead to a deterioration in the mechanical properties (Figure 5h). The TTA with multi-coordination mode slowed down the relaxation dynamics by interfering with the reorganization of metal-ligand bonds, resulting in lower tensile strength, and better stretchability.[37] As a result, based on the light-triggered shape memory and fluorescence properties of PU-PEu/TTA, a fluorescent "flower" was fixed into a temporary "bud" via a heating-cooling process, and then the flower was blooming again through NIR irradiation. (Figure 5i; Movie S1, Supporting Information).

2.5. 3D Information Encryption Device & Light-Writing

Compared with the conventional 2D information encryption devices with predictable readout processes, the 3D information encryption devices with enhanced encryption complexity greatly increased the difficulty of forging information.[38] Whereas, the fabrication of such devices with advanced encryption features remained challenging. Relying on the customizable photothermal / fluorescence properties, light-triggered shape memory, and photoweldability, the integrated 3D fluorescence encryption device constructed by PU-PFe and PU-PEu/TTA has been successfully manufactured, which performed spatial selective encryption (**Figure 6**a). The 3D fluorescent encryption device was based on the "segment display font" principle (Figure S21, Supporting information). First, seven pieces of fluorescent PU-PEu/TTA films were welded in parallel on the PU-PFe film to display the number "8". Subsequently, seven pieces of PU-PFe films were welded to the side of each piece of PU-PEu film at an angle perpendicular to the bottom PU-PFe to ensure that the corresponding fluorescent film can be shielded through the deformation. Note that the seven fluorescent PU-PEu/TTA films were marked "red/orange/yellow/green/cyan/blue/purple" to correspond to the input code "1/2/3/4/5/6/7" (Figure 6b). Based on the NIR-triggered shape memory, selective NIR exposure to seven regions according to different input codes can display different output codes, thus decryption. For instance, the input code "[3-6]–1-[4-7]–2-5" can be used to decrypt the output message "1-7-3-9-8" (Figure 6c). This output code can be de-

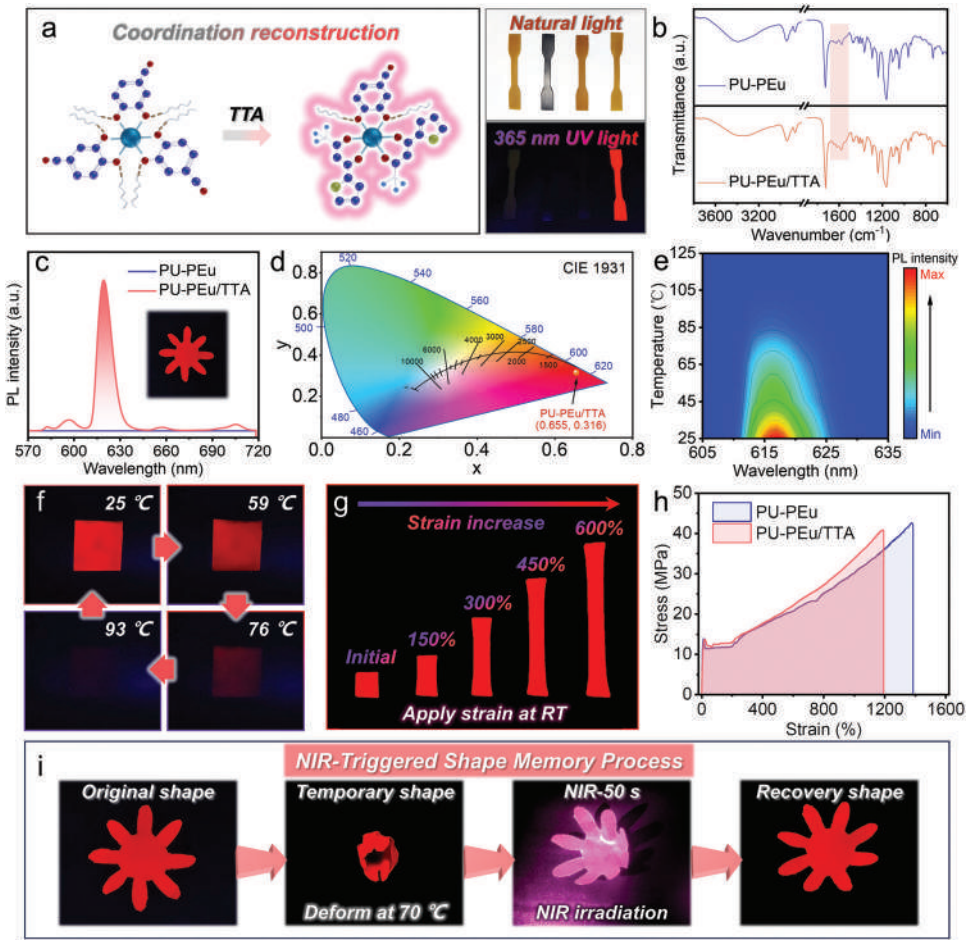

Figure 5. Customized PU-PEu/TTA film with tunable fluorescence and light-triggered shape memory. a) Schematic of customized fluorescent PU-PEu/TTA film based on coordination reconstruction involving functional ligands. Insets were photographs of the various PU films under natural light and 365 nm UV light. b) FTIR spectra of PU-PEu and PU-PEu/TTA films. c) Fluorescence spectra of PU-PEu and PU-PEu/TTA films excited at 365 nm. d) CIE chromaticity diagram of PU-PEu/TTA film. e) In situ fluorescence spectra of PU-PEu/TTA films at different temperatures. f) A demonstration of PU-PEu/TTA film with thermal-responsive fluorescence under UV excitation. g) Photographs of PU-PEu/TTA film at various strains excited 365 nm UV light. h) Engineering stress-strain curves of PU-PEu and PU-PEu/TTA films. i) Images of the fluorescent "blooming flower process" based on NIR-triggered shape memory.

crypted in the following order: first, NIR ligt irradiated the regions marked "yellow/blue", then "red", "green/violet", "orange", and finally "cyan". The photo-welded 3D information encryption device exhibited a unique photomechanically modulated fluorescence mechanism and had the advantage of remote-control precision, which was expected to be applied to important data storage in the economic and military fields.

Furthermore, smart rewritable display systems based on reversible stimulus-responsive materials were widely studied to reduce the heavy consumption of electronic disposables in the Internet of Things era.[39] The PU-PEu/TTA film with intrinsic photothermal and thermal-responsive fluorescence properties can be directly employed as a smart rewritable display system without relying on a sophisticated designed multistage structure (Figure 6d). Based on the "light input-heat generation-fluorescence output" process, various texts can be written on the PU-PEu/TTA film by manually controlling the movement locus of the facula from the 808 nm laser. Subsequently, the letter "H" was written on the surface of the PU-PEu/TTA film using an 808 nm laser pointer as the "pen". After the NIR laser was turned off, the temperature dropped rapidly causing the written information to self-erasing after 30 s. Benefiting from the excellent thermal stability of the PU-PEu/TTA film, this smart rewriting system exhibited superior "laser writing/self-erasing/laser rewriting" capabilities. As shown in Figure 6e, the text of "H", "I", and "T" could be written orderly using the laser at the same position on the PU-PEu/TTA film.

3. Conclusion

This work demonstrated how to tailor multifunctional shape memory polymers toward diverse shape-shifting-related intelligent systems by exploiting MPS without to be restricted to the polymer's mechanical properties, manufacturability, and functional integration strategies. Benefiting from the supramolecular properties, the MPS-cored polymer network exhibited cus-

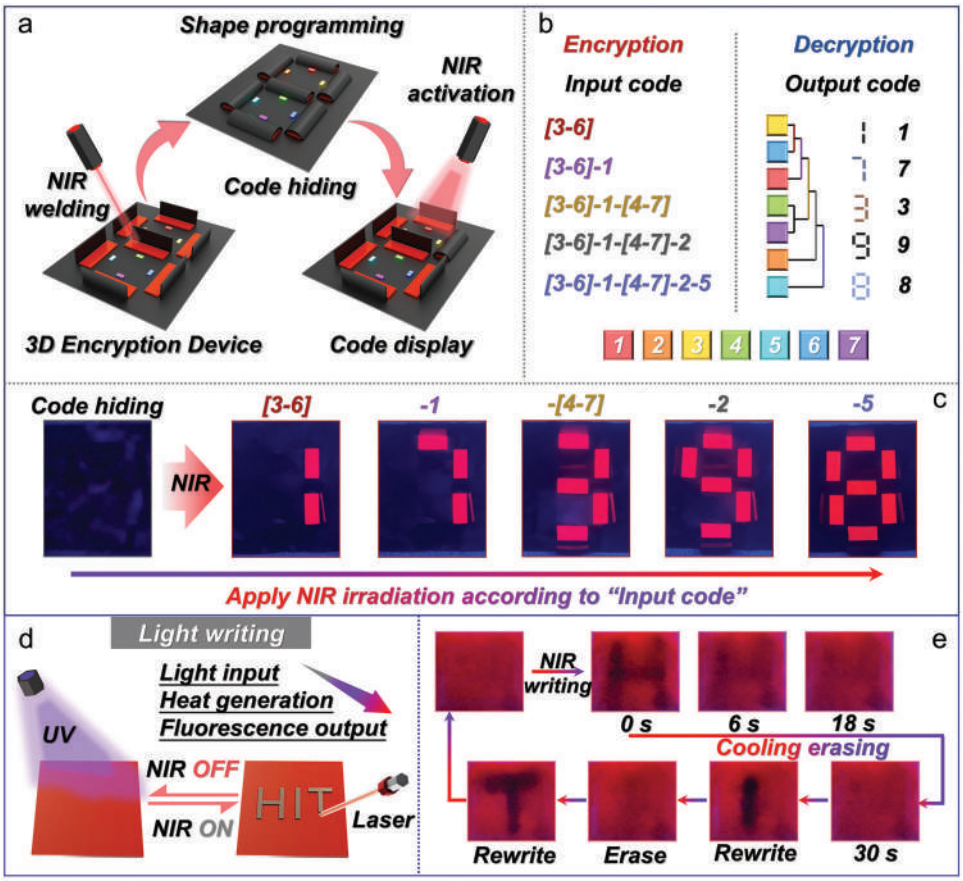

Figure 6. Photo-welding 3D information encryption device and direct light-writing display system. a) Schematic illustration showing the manufacturing process of the 3D information encryption device based on photo-welding. b) The design of a corresponding encryption-decryption program. c) The illustration showing the decryption process of the output code "1-7-3-9-8" based on NIR irradiation according to the input code "[3-6]−1-[4-7]−2-5″. d) Schematic diagram of the NIR-writing. e) Photographs of the NIR-writing and rewriting process on the PU-PEu/TTA films.

tomizable intrinsic photothermal/tunable fluorescence, photo-weldability, shape memory effect, and high toughness. Photo-weldability provided convenience for processing multi-materials in integrated architectures. Personalized 4D devices composed of various functional polymers could be rapidly manufactured by photo-welding instead of 4D printing and served complex application scenarios. As proof-of-concept, the shape memory stent made quickly by photo-welding provided a reference for the flexible customization of medical devices in emergency rescue. The photo-welded 3D information encryption device provided a template for the construction of a high-security anti-counterfeiting platform. This work not only provided a powerful solution to develop multifunctional smart materials but also demonstrated a flexible concept for the design and manufacture of personal 4D devices. This function integration strategy based on assembled MPS will also improve the adaptability of shape memory polymers in diverse applications.

Supporting Information

Supporting Information is available from the Wiley Online Library or from the author.

Acknowledgements

This work was supported by the National Key R&D Program of China (2022YFB3805700) and the National Natural Science Foundation of China (11902099).

Conflict of Interest

The authors declare no conflict of interest.

Data Availability Statement

Research data are not shared.

Keywords

intelligent devices, intrinsic photoresponsive, metal-phenolic systems, photo-welding, shape memory polymers

Received: February 10, 2024
Revised: March 18, 2024
Published online:

[1] A. Rose, Z. Zhu, C. F. Madigan, T. M. Swager, V. Bulović, *Nature* **2005**, *434*, 876.
[2] a) H. Xuan, Q. Guan, H. Tan, H. Zuo, L. Sun, Y. Guo, L. Zhang, R. E. Neisiany, Z. You, *ACS Nano* **2022**, *16*, 16954; b) L. Zhang, X. Huang, T. Cole, H. Lu, J. Hang, W. Li, S.-Y. Tang, C. Boyer, T. P. Davis, R. Qiao, *Nat. Commun.* **2023**, *14*, 7815.
[3] a) J. Huang, Y. Jiang, Q. Chen, H. Xie, S. Zhou, *Nat. Commun.* **2023**, *14*, 7131; b) Y. Shen, X. Le, Y. Wu, T. Chen, *Chem. Soc. Rev.* **2024**, *53*, 606; c) C. Li, J. Liu, X. Qiu, X. Yang, X. Huang, X. Zhang, *Angew. Chem., Int. Ed.* **2023**, *62*, 202313971.
[4] Y. Yang, Z. Pei, Z. Li, Y. Wei, Y. Ji, *J. Am. Chem. Soc.* **2016**, *138*, 2118.
[5] a) H. Liang, S. Zhang, Y. Liu, Y. Yang, Y. Zhang, Y. Wu, H. Xu, Y. Wei, Y. Ji, *Adv. Mater.* **2022**, *35*, 2202462; b) Y. Wu, S. Zhang, Y. Yang, Z. Li, Y. Wei, Y. Ji, *Sci. Adv.* **2022**, *8*, eabo6021.
[6] a) C. Chen, X. Zhao, Y. Chen, W. Chu, Y. Wu, Y. Zhao, P. Shi, W. Chen, H. Li, X. He, H. Liu, *Nano Lett.* **2022**, *22*, 8413; b) M. Chen, Y. Hou, R. An, H. J. Qi, K. Zhou, *Adv. Mater.* **2023**, 2303969; c) J. Gu, X. Zhang, H. Duan, M. Wan, H. Sun, *Int. J. Smart Nano Mater.* **2021**, *12*, 286.
[7] a) S. Tian, S. J. D. Lugger, C.-S. Lee, M. G. Debije, A. P. H. J. Schenning, *J. Am. Chem. Soc.* **2023**, *145*, 19347; b) J. Wang, R. Yan, Y. Hu, G. Du, G. Liao, H. Yang, Y. Luo, X. Zheng, Y. Chen, S. Wang, X. Li, *Angew. Chem., Int. Ed.* **2021**, *61*, e202112290.
[8] a) J. Chen, R. An, W. S. Tey, Q. Zeng, L. Zhao, K. Zhou, *Adv. Sci.* **2023**, *10*, 2300593; b) X. Liu, K. Pang, H. Qin, Y. Liu, Y. Liu, C. Gao, Z. Xu, *ACS Nano* **2022**, *16*, 14703; c) S. Yang, Y. He, J. Leng, *Int. J. Smart Nano Mater.* **2022**, *13*, 1.
[9] a) M. Kalaj, K. C. Bentz, S. Ayala, J. M. Palomba, K. S. Barcus, Y. Katayama, S. M. Cohen, *Chem. Rev.* **2020**, *120*, 8267; b) R. Liang, H. Yu, L. Wang, N. Wang, B. U. Amin, *Adv. Funct. Mater.* **2021**, *31*, 2102621.
[10] a) P. Bertsch, M. Diba, D. J. Mooney, S. C. G. Leeuwenburgh, *Chem. Rev.* **2022**, *123*, 834; b) E. Khare, N. Holten-Andersen, M. J. Buehler, *Nat. Rev. Mater.* **2021**, *6*, 421.
[11] a) K. Gao, Q. Feng, Z. Zhang, R. Zhang, Y. Hou, C. Mu, X. Li, M. Zhang, *Angew. Chem., Int. Ed.* **2022**, *61*, e202209958; b) J. Liu, J. Li, S. Qiao, Z. Wang, P. Zhang, X. Fan, P. Cheng, Y. S. Li, Y. Chen, Z. Zhang, *Angew. Chem., Int. Ed.* **2022**, *61*, e202212253.
[12] H. Ejima, J. J. Richardson, F. Caruso, *Nano Today* **2017**, *12*, 136.
[13] J. Guo, Y. Ping, H. Ejima, K. Alt, M. Meissner, J. J. Richardson, Y. Yan, K. Peter, D. von Elverfeldt, C. E. Hagemeyer, F. Caruso, *Angew. Chem., Int. Ed.* **2014**, *53*, 5546.
[14] Z. Wang, J. Gao, J. Zhou, J. Gong, L. Shang, H. Ye, F. He, S. Peng, Z. Lin, Y. Li, F. Caruso, *Adv. Mater.* **2022**, *35*, 2209015.
[15] A. H. Agergaard, A. Sommerfeldt, S. U. Pedersen, H. Birkedal, K. Daasbjerg, *Angew. Chem., Int. Ed.* **2021**, *60*, 21543.
[16] K. Xu, C. Mu, C. Zhang, S. Deng, S. Lin, L. Zheng, W. Chen, Q. Zhang, *Biomaterials* **2023**, *301*, 122268.
[17] H. Ejima, J. J. Richardson, K. Liang, J. P. Best, M. P. v. Koeverden, G. K. Such, J. Cui, F. Caruso, *Science* **2013**, *341*, 154.
[18] A. Lendlein, R. Langer, *Science* **2002**, *296*, 1673.
[19] S. Wu, J. Huang, S. Jing, H. Xie, S. Zhou, *Adv. Funct. Mater.* **2023**, *33*, 2303292.
[20] a) F. Zhang, N. Wen, L. Wang, Y. Bai, J. Leng, *Int. J. Smart Nano Mater.* **2021**, *12*, 375; b) W. Zhao, J. Zhu, L. Liu, J. Leng, Y. Liu, *Int. J. Smart Nano Mater.* **2023**, *14*, 1.
[21] M. Krogsgaard, M. R. Hansen, H. Birkedal, *J. Mater. Chem. B* **2014**, *2*, 8292.
[22] N. Holten-Andersen, M. J. Harrington, H. Birkedal, B. P. Lee, P. B. Messersmith, K. Y. C. Lee, J. H. Waite, *Proc. Natl. Acad. Sci. U.S.A.* **2011**, *108*, 2651.
[23] a) W. Du, Y. Jin, L. Shi, Y. Shen, S. Lai, Y. Zhou, *Composites, Part B* **2020**, *195*, 108092; b) Q. Li, H. He, X. Ye, F. Guan, Y. Ai, Y. Shen, C. Zhang, *Chem. Eng. J.* **2023**, *475*, 146500.
[24] a) X. Chen, R. Wang, C. Cui, L. An, Q. Zhang, Y. Cheng, Y. Zhang, *Chem. Eng. J.* **2022**, *428*, 131212; b) M. Cui, C. Tian, Y. Yang, L. Huang, Q. Liu, N. Yang, F. Zhao, X. Cai, W. Kong, *Chem. Eng. J.* **2023**, *475*, 146091; c) J. Wang, X. Lin, R. Wang, Y. Lu, L. Zhang, *Adv. Funct. Mater.* **2022**, *33*, 2211579.
[25] a) X. Wang, J. Xu, Y. Zhang, T. Wang, Q. Wang, S. Li, Z. Yang, X. Zhang, *Nat. Commun.* **2023**, *14*, 4712; b) Y. Yao, Z. Xu, B. Liu, M. Xiao, J. Yang, W. Liu, *Adv. Funct. Mater.* **2020**, *31*, 2006944; c) Z. H. Zhao, P. C. Zhao, S. Y. Chen, Y. X. Zheng, J. L. Zuo, C. H. Li, *Angew. Chem., Int. Ed.* **2023**, *62*, e202301993; d) X. Zhou, L. Wang, Z. Wei, G. Weng, J. He, *Adv. Funct. Mater.* **2019**, *29*, 1903543.
[26] Z. Tong, Y. Xie, M. C. Arno, Y. Zhang, I. Manners, R. K. O'Reilly, A. P. Dove, *Nat. Chem.* **2023**, *15*, 824.
[27] Y. Li, S. Chen, M. Wu, J. Sun, *ACS Appl. Mater. Interfaces* **2014**, *6*, 16409.
[28] Y. Liang, Z. Li, Y. Huang, R. Yu, B. Guo, *ACS Nano* **2021**, *15*, 7078.
[29] L. Zhao, Y. Liu, R. Xing, X. Yan, *Angew. Chem., Int. Ed.* **2019**, *59*, 3793.
[30] Z. Ping, H. Fang, K. Wang, H. Zhang, S. Li, J. Chen, F. Huang, *Adv. Funct. Mater.* **2022**, *32*, 2208965.
[31] Z. Pei, Y. Yang, Q. Chen, Y. Wei, Y. Ji, *Adv. Mater.* **2015**, *28*, 156.
[32] Y. Wang, H. Cui, T. Esworthy, D. Mei, Y. Wang, L. G. Zhang, *Adv. Mater.* **2022**, *34*, 2109198.
[33] C. Ni, D. Chen, Y. Yin, X. Wen, X. Chen, C. Yang, G. Chen, Z. Sun, J. Wen, Y. Jiao, C. Wang, N. Wang, X. Kong, S. Deng, Y. Shen, R. Xiao, X. Jin, J. Li, X. Kong, Q. Zhao, T. Xie, *Nature* **2023**, *622*, 748.
[34] a) K. Xue, C. Wang, J. Wang, S. Lv, B. Hao, C. Zhu, B. Z. Tang, *J. Am. Chem. Soc.* **2021**, *143*, 14147; b) H. Zhang, Q. Li, Y. Yang, X. Ji, J. L. Sessler, *J. Am. Chem. Soc.* **2021**, *143*, 18635.
[35] G. Weng, S. Thanneeru, J. He, *Adv. Mater.* **2018**, *30*, 1706526.
[36] J. B. Beck, S. J. Rowan, *J. Am. Chem. Soc.* **2003**, *125*, 13922.
[37] H. Park, T. Kang, H. Kim, J.-C. Kim, Z. Bao, J. Kang, *Nat. Commun.* **2023**, *14*, 5026.
[38] C. Yang, H. Xiao, L. Tang, Z. Luo, Y. Luo, N. Zhou, E. Liang, G. Wang, J. Tang, *Mater. Horiz.* **2023**, *10*, 2496.
[39] S. Wei, W. Lu, H. Shi, S. Wu, X. Le, G. Yin, Q. Liu, T. Chen, *Adv. Mater.* **2023**, *35*, 2300615.